Greenhouse gases modulate the strength of millennial-scale subtropical rainfall, consistent with future predictions

Fei Guo[1,2,3*], Steven C. Clemens[3,*], Yuming Liu[2,4], Ting Wang[2,4], Huimin Fan[2], Xingxing Liu[2], Youbin Sun[2,5,6]

[1]Institute of Marine Science and Technology, Shandong University, Qingdao 266237, China

[2]State Key Laboratory of Loess and Quaternary Geology, Institute of Earth Environment, Chinese Academy of Sciences, Xian 710061, China

[3]Department of Earth, Environmental, and Planetary Sciences, Brown University, Providence, RI 02912-1846, USA

[4]University of Chinese Academy of Sciences, Beijing 100049, China

[5]CAS Center for Excellence in Quaternary Science and Global Change, Xian 710061, China

[6]Open Studio for Oceanic-Continental Climate and Environment Changes, Pilot National Laboratory for Marine Science and Technology (Qingdao), Qingdao 266200, China

Corresponding author: Fei Guo (guofei@ieecas.cn) and Steven C. Clemens (steven_clemens@brown.edu)

Highlights

The new precipitation-sensitive proxy (Ca/Ti) shows persistent millennial-scale East Asian summer monsoon changes over past 650 ka;

The magnitude of millennial-scale variability is modulated by AMOC at the eccentricity and precession bands;

Increasing GHG and strong insolation lead to more frequent occurrence of extreme rainfall, consistent with model results.

Abstract: Millennial-scale East Asian monsoon variability is closely associated with natural hazards through long-term variability in flood and drought cycles. Therefore, exploring what drives the millennial-scale variability is of significant importance for future prediction of extreme climates. Here we present a new East Asian summer monsoon (EASM) rainfall reconstruction from the northwest Chinese loess plateau spanning the past 650 ka. The magnitude of millennial-scale variability (MMV) in EASM rainfall is linked to ice volume and greenhouse gas (GHG) at the 100-kyr earth-orbital eccentricity band and to GHG and summer insolation at the precession band. At the glacial-interglacial cycle, gradual changes in CO_2 at times of intermediate ice volume leads to increased variability in North Atlantic stratification and Atlantic meridional overturning circulation, propagating abrupt climate changes into East Asia via the westerlies. Within the 100-kyr cycle precession variability further enhances the response, showing that stronger insolation and increased atmospheric GHG cause increases in the MMV of EASM rainfall. These findings indicate increased extreme precipitation events under future warming scenarios, consistent with model results.

Key words: EASM rainfall, MMV, GHG modulation, precession band

1. Introduction

Chinese loess is a unique terrestrial archive that can well document East Asian monsoon (EAM) variability at tectonic to millennial timescales (Porter and An, 1995; An et al., 2011). High-resolution loess records have revealed persistent millennial-scale (1-10 kyr periodicity) EAM fluctuations spanning the last several glacial cycles (Guo et al., 1996; Sun et al., 2012, 2021a,b; Guo et al., 2021), which are dynamically linked with high-latitude abrupt changes in the north Atlantic including Heinrich (H) (Heinrich, 1988) and Dansgaard-Oeschger (DO) events (Dansgaard et al., 1982). This millennial-scale monsoon variability is superimposed on glacial-interglacial variations (Ding et al., 1999; Clemens et al., 2018). Abrupt summer monsoon changes are closely linked to natural hazards such as flood and drought events (Huang et al., 2007), since the summer monsoon plays a leading role in transporting water vapor from low to middle/high latitudes of the northern hemisphere (Liu et al., 2013; An et al., 2015). Abrupt rainfall events associated with short-term summer monsoon variations strongly influence agriculture, food production, water supply and social economic development (Huang et al., 2007; Cook et al., 2010; Li et al., 2017). However, how these flood/drought events are affected by both natural and anthropogenic factors remains poorly constrained. Understanding the mechanisms that modulate the magnitude of millennial-scale variability (MMV) is of critical importance for the scientific community as well as policy makers. Here we use the term “modulate” in the context of lower-frequency components of the climate system influencing or determining the amplitude of a higher-frequency components.

A number of well-dated, high-resolution speleothem $\delta^{18}O$ records have been developed in recent years (Wang et al., 2008; Cheng et al., 2016), providing the opportunity to examine the underlying relationship(s) between East Asian monsoon MMV and potential longer-term (orbital-scale) modulators. The latest research suggests that the MMV through the Pleistocene is influenced by both glacial boundary condition and orbital configurations (Sun et al., 2021b). Cheng et al., (2016) hypothesized, on the basis of an East Asian composite speleothem $\delta^{18}O$ record ($\delta^{18}Osp$), that periods of maximum Northern Hemisphere summer insolation correspond to weaker millennial-scale variability. Subsequently, however, Thirumalai et al (2020) showed that precession does not modulate the MMV of δ^{18}Osp and postulated that it is, instead, modulated by internal processes related to the cryosphere. This work also raised the possibility that δ^{18}Osp is decoupled from regional Asian monsoon rainfall over millennial timescales (Zhang et al., 2018). As such, two important outstanding questions remain; is there a reliable proxy for East Asian summer monsoon (EASM) rainfall at the millennial timescale and what factors modulate the MMV thereof?

Due to weak pedogenesis and high sedimentation rates, millennial-scale oscillations are well preserved in the western and northwestern Chinese Loess Plateau (CLP) over the past glacial cycles (Sun et al., 2012, 2021a; Guo et al., 2021). The Linxia profile is well-suited for reconstructing rapid monsoon changes because it is located in monsoon frontal zone and sensitive to high- and low-latitude climate variability. To address the above questions, we have generated a high-resolution summer monsoon proxy (Ca/Ti) from Linxia on the western CLP (Fig. 1). The Ca/Ti ratio is a precipitation-sensitive proxy linked to summer monsoon rainfall (Guo et al., 2021). Low values of Ca/Ti indicate stronger Ca leaching associated with intensified summer rainfall. The new precipitation proxy (Ca/Ti) and δ^{18}Osp are evaluated to elucidate the modulating drivers of these two proxy records. As discussed in the Results section, we find that the MMV of Ca/Ti is mainly modulated by ice volume and greenhouse gases (GHG) at the eccentricity band. Both GHG and summer insolation modulate the MMV of Ca/Ti at the precession band but not that of δ^{18}Osp; δ^{18}Osp MMV is modulated by winter insolation at the eccentricity and obliquity bands. The interpretations of these results are presented in the Discussion section.

2. Materials and Methods

2.1 Site and measurements of loess sections

The Linxia (LX; 103.63°E, 35.15°N, 2,200 m a.s.l.) loess record is from the western edge of the CLP (Fig. 1). At present, mean annual temperature and precipitation in this region are about 8.1°C and 484 mm, respectively, with ~80% of the annual precipitation falling during the summer season (May to September). The 203.8 m-long core A (LXA) consists of 185 m of eolian loess-paleosol sequences, underlain by 17 m of fluvial loess and 1.8 m of sandy gravel layers. The 72 m-long core B (LXB) and a 7 m pit were excavated in 2017. Powder samples were collected at 2 cm intervals for analyzing mean grain size (MGS) with the resolution ranging 10~200 yr/cm. As well, 2-cm resolution samples were dried at 40°C overnight and ground to 200 mesh size (about <75 μm) with an agate mortar and pestle, and then pressed into a plastic sheet (4 cm × 4 cm × 0.3 cm), creating a flat and homogeneous slide. The plastic slides were then placed on a wood pallet for XRF scanning to obtain elemental intensities (Guo et al., 2021).

2.2 Age model and evaluations of age uncertainties

删除[SClemens]: **influence**

The chronological framework for Chinese loess-paleosol sequences is widely constructed by matching grain-size to benthic LR04 $\delta^{18}O$ records (Porter and An, 1995; Hao et al., 2012; Sun et al., 2021a). A similar approach utilizes correlation to speleothem $\delta^{18}O$ in recent years (Beck et al., 2018; Sun et al., 2021a; Zhang et al., 2022). The age model of Linxia profile is generated by synchronizing Chinese loess and speleothem $\delta^{18}O$ records back to 650 ka (published by Sun et al., in 2021a). Detailed information of loess/paleosol strata is showed in Fig. 2 and refers to Sun et al. (2021a). The first set of control points tie the loess/paleosol boundaries S_6 to S_0 to the timing of the glacial terminations/inceptions in speleothem $\delta^{18}O$ (Cheng et al., 2016). The second and third sets of age control points tie the timing of precessional transition boundaries and abrupt cooling events in the MGS record to those in speleothem $\delta^{18}O$ (Fig. 2b), based on the assumption that the

删除[郭飞]: d18O

删除[SClemens]: using an independent loess chronology generated

删除[SClemens]:

East Asian summer and winter monsoon co-vary at orbital timescales, and millennial-scale abrupt events are synchronous in the northern hemisphere (Hemming et al., 2004; Sun et al., 2012; Clemens et al., 2018). The tie points are shown in Fig. 2b.

The composite speleothem $\delta^{18}O$ record is well resolved by absolute U-Th dating and applied as the target for regional synchronization. The errors are less than 2 kyr for the last 450 ka and increase to 4-8 kyr before 450 ka (Cheng et al., 2019). The MGS record yields good correlation between loess/paleosol boundaries and glacial/interglacial transitions of LR04 $\delta^{18}O$. The age differences of most glacial terminations are around 2-4 kyr (Fig. 2b, Sun et al., 2021a) with sedimentation rate ranging from 5-100 cm/kyr. The speleothem $\delta^{18}O$ synchronized age model is compared with benthic $\delta^{18}O$ age model to evaluate the influence of age uncertainties on the wavelet coherence analysis. The small differences in the two age models (correlation to marine $\delta^{18}O$ and to speleothem $\delta^{18}O$) make little difference in the MMV and associated wavelet coherence (WTC). This is because age model tie points are separated by 20-30 kyrs and the small differences in the tie-points among the two age models has little to no influence on the amplitude (MMV) of millennial-scale peaks. Only minor differences in the MMV WTC phase are observed at the obliquity (450-550 ka) and precession bands (100-200 ka). (Compare Fig. S1 with Fig. 4).

2.3 Spectrum and wavelet coherence analysis

In order to estimate the MMV, loess Ca/Ti and $\delta^{18}O_{sp}$ are linear interpolated at 0.1 kyr interval. The WTC results remain unchanged unless the cutoff threshold is reduced to to 6 kyr or increased it to 12 kyr; then original time series are filtered using a Butterworth filter at a cutoff threshold of 10 kyr (e.g. Ca/Ti-hi-10kyr). The moving standard deviation of millennial-scale variability is calculated to ascertain the orbitally-related modulation and its association with internal and

删除[SClemens]: Since t
删除[郭飞]: are
删除[SClemens]: ly
删除[郭飞]: method
删除[SClemens]: comparison
删除[郭飞]:
删除[SClemens]: , t
删除[郭飞]: ary
删除[郭飞]: new
删除[郭飞]: are
删除[郭飞]: tuning
删除[SClemens]: The millennial-scale components of loess Ca/Ti at the different age model are isolated for further comparison, showing that (Fig. S1). Tthe age differences of millennial-scale signals is 1-2less than 2 kyr
删除[郭飞]:
删除[郭飞]: d18O
删除[郭飞]:
删除[郭飞]: d18O
删除[SClemens]: B
删除[SClemens]: the
删除[郭飞]:
删除[SClemens]: (Fig. S1)
删除[郭飞]:

external forcing using 2 kyr sliding window (calculation method follows Thirumalai et al., 2020). The spectra of all proxies were calculated using the Lomb-Scargle periodogram (https://exoplanetarchive.ipac.caltech.edu/cgi-bin/Pgram/nph-pgram), which has the advantage of analyzing discontinuous time series and removal of spurious spectral characteristics (VanderPlas, 2018). Normalized and combined orbital parameters eccentricity, tilt, and negative precession (ETP), GHG, insolation, and benthic $\delta^{18}O$ were evaluated by WTC to extract maximal phase and amplitude correlations with astronomical, ice volume and greenhouse gases forcing over the past 650 ka. WTC between time series was performed in a Monte Carlo framework (n = 1, 000) following Grinsted et al., (2004). The WTC would help to detect the period in different frequency bands where the two time series co-vary (but does not necessarily have high power). The black arrows in the figures represent the phrase relationship between the two time sequences with rightward, upward and downward arrows indicate the in-phrase, leading and lagging phrase, respectively. The colour scale indicates the amplitude correlations between the two datasets.

In this paper, the parameter ΔRF_{GHG} is regarded as GHG radiative forcing (GHG RF, using the GHG RF instead of ΔRF_{GHG} in the discussion section) and applied in WTC to evaluate the relationship between MMV of Ca/Ti and $\delta^{18}O$ sp. The ΔRF_{GHG} is reconstructed by referencing the content of EPICA ice core greenhouse gases to the modern value. ΔRF_{GHG} is defined as the difference between a certain past GHG level ($[CO_2]$ and $[CH_4]$) and the pre-industrial greenhouse gas level ($[CO_2]_0 = 280$ ppm, $[CH_4]_0 = 700$ ppb) (Ramaswamy et al., 2001). While CH_4 contributes <5%, we calculated the ΔRF_{GHG} using both CO_2 and CH_4. The equation used to determine ΔRF_{GHG} is as follows (Lo et al., 2017):

$$\Delta RF_{GHG} = \Delta RF_{CO2} + \Delta RF_{CH4}$$

$$= 4.841\ln([CO_2]/[CO_2]_0) + 0.0906(\sqrt{[CO_2]} - \sqrt{[CO_2]_0}) + 0.036\ln(\sqrt{[CH_4]} - \sqrt{[CH_4]_0})$$

3. Results

The MGS reflects grain-size sorting and is very sensitive to winter monsoon variations (Porter and An, 1995; Sun et al., 2006) with larger particle size during the glacials. The Ca/Ti ratio reflects precipitation-induced leaching intensity linked to summer monsoon rainfall (Guo et al., 2021), with lower value during the interglacials. The high resolution $\delta^{18}O$ of Sanbao-Hulu speleothem is an indicator of EASM changes at orbital to centennial timescales (Cheng et al., 2016). The MGS and Ca/Ti exhibit distinct glacial-interglacial and precessional variations over the last 650 ka as seen in LR04 $\delta^{18}O$ (Lisiecki and Raymo, 2005) and speleothem $\delta^{18}O$ (Cheng et al., 2016), respectively (Fig. 2b).

Both Ca/Ti and $\delta^{18}Osp$ records show clear millennial-scale fluctuations overlaying orbital-scale variations. The high frequency millennial signals (Materials and Methods) persist over the last 650 ka, but the amplitude varies from proxy to proxy (Fig. 3a and S2a). Spectral analysis of the raw records and MMV for loess and speleothem records display variable associations with eccentricity- (~100 kyr), obliquity- (~41 kyr), and precession-scale (~23 and ~19 kyr) over the past 650 ka. Loess Ca/Ti variance is mainly concentrated in obliquity with lesser variance in the eccentricity and precession bands (Fig. 3b), indicating prominent ice volume (eccentricity and obliquity) and isolation (precession) forcing. The speleothem $\delta^{18}O$ shows predominant precession-scale variance (Fig. S2b) suggesting strong links to insolation forcing (Cheng et al., 2016). These results indicate ice volume and insolation play dominant roles in driving changes in loess Ca/Ti and speleothem $\delta^{18}O$, respectively (Cheng et al., 2016; Sun et al., 2021a).

Millennial-scale fluctuations co-exist with long-term orbital- and ice-volume variability; we seek to assess the potential linkages among them and in particular, the extent to which MMV is modulated by these longer-term orbital and internal climate parameters. The spectra of Ca/Ti MMV shows dominant eccentricity with less strong precession and weak obliquity variance (Fig. 3d). The spectrum of δ^{18}Osp MMV has a small peak near 100 kyr and an offset 41 kyr peak with little to no variance at the 23 kyr period (Fig. S2d). Thus, while both proxies are similarly modulated at the 100-kyr period (such that the MMV is larger during glacial intervals relative to interglacial times) the MMV modulation is variable for the two proxies at other orbital bands.

As with the spectral differences in the raw records, the MMV spectra also implies different MMV modulating drivers, potentially associations with insolation, ice volume, and/or GHG (Thirumalai et al., 2020). How do internal and external drivers interact with each other and modulate the MMV of these records at the orbital timescale? We performed wavelet coherence and phase analyses of both MMV records relative to ETP, ice volume, ΔRF_{GHG}, summer insolation, and winter insolation to identify which variables might modulate the MMV of these EASM records. The MMV in Ca/Ti is strongly coherent with ice volume and GHG at the 100,000-year earth-orbital eccentricity band and with GHG and summer insolation at the 23,000-year precession band (Fig. 4c, d, g). δ^{18}Osp MMV is most strongly coherent with GHG and ice volume at the 100-kyr band and with winter insolation at the eccentricity and obliquity bands (Fig. S3c, d, g).

4. Discussion

4.1 Orbital-scale modulation factors for MMV of the EASM

Previous geological records and modeling indicate that high latitude ice volume or ice sheet topography play important roles in triggering abrupt climate changes (Broecker et al.,1994; Clark et al., 2001). In particular, abrupt climate changes are highly sensitive to ice volume variations; ice sheets are widely hypothesized to motivate and amplify these high frequency signals within a constrained benthic oxygen isotope-“ice volume threshold” between 3.5 and 4.5‰ (Bailey et al., 2010; Naffs et al., 2013; Zhang et al., 2014). Wavelet coherence between the MMV of loess Ca/Ti, speleothem $\delta^{18}O$ and the global benthic $\delta^{18}O$ stack show excellent coherence and near-zero phase with ice volume at the 100 kyr band (Fig. 4e, g and S3e, g); this in-phase variation demonstrates that EASM MMV primarily follows the glacial-interglacial rhythm of ice volume variations, enlarged during glacial times and dampened during interglacial times. However, coherence of the MMV for these two proxies with the benthic $\delta^{18}O$ stack is relatively weak and variable at the 41 kyr band ($\delta^{18}O_{sp}$; Fig. S3e, g) and 23-kyr band (Ca/Ti; Fig. 4e, g). These relationships demonstrate that ice volume directly modulates the MMV of the EASM, predominantly at the 100 kyr band, with high ice volume corresponding to larger MMV.

GHG concentration is another potential driver of abrupt climate changes (Alvarez-Solas et al., 2011; Zhang et al., 2017).Wavelet coherence between the MMV of loess Ca/Ti, speleothem $\delta^{18}O$ and the record of GHG RF show excellent coherence and ~180° phase at the 100-kyr eccentricity band (Fig. 4b, d and S3b, d) indicating strong MMV at times of low GHG. Given the coupled nature of global ice-volume and atmospheric GHG, it is clear that over the late Pleistocene glacial-interglacial cycles, these two factors modulate the MMV of the EASM as recorded by Ca/Ti and speleothem $\delta^{18}O$ such that abrupt climate change is amplified during times of high ice volume and low GHG concentration. However, this is not the case for the precession band. MMV of loess Ca/Ti displays discrete intervals high coherence and near-zero phase with GHG RF at the precession band (Fig. 4b, d), which is not the case for speleothem $\delta^{18}O$ (Fig. S3b, d). Thus, GHG RF does play a role in modulating Ca/Ti MMV but not that of $\delta^{18}O_{sp}$ at the precession band, indicating a difference in the millennial-scale response of these two proxies at this time-scale. We investigate this further by assessing the response to local insolation forcing.

The MMV of Ca/Ti show discontinuous relatively weak coherence with 35°N summer insolation at the precession band with even weaker coherence at the 41-kyr band (Fig. 4a, c); we note that the summer insolation modulation is less strong relative to that of GHG at the precession band (Fig. 4b, d). In contrast, the MMV of δ^{18}Osp displays high coherence and zero phase with 35°N winter insolation at 100 kyr period, relatively weaker coherence, with a lagging phase, at the 41 kyr band, and negligible coherence at the 23-ky band (Fig. S3a, c). These results indicate that the MMV of speleothem δ^{18}O is modulated by local winter insolation, opposite to the Cheng et al., (2016) hypothesis calling on north hemisphere summer insolation.

4.2 Mechanism and implication for modulation of EASM MMV

At the glacial-interglacial timescale, the MMV is amplified under the glacial boundary conditions. This indicates dynamic linkages with high latitude North Atlantic Heinrich and DO events (Cheng et al., 2016; Sun et al., 2012, 2021a, b). Heinrich and DO variability are linked to Northern Hemisphere ice sheet (NHIS) perturbations via its influence on fresh-water flux into the North Atlantic Ocean and consequent Atlantic meridional overturning circulation (AMOC) changes (McManus et al., 1999; Hemming, 2004; Naffs et al., 2013). At times of intermediate ice sheet volume, minor changes in NHIS height and atmospheric CO_2 concentrations can trigger the rapid climate transitions (Zhang et al., 2014, 2017). Altering the height of NHIS leads to changes in the gyre circulation and sea-ice coverage by shifting the northern westerlies (Zhang et al., 2014). The maximum westerly wind stress shifts northwards associated with gradual increase of the Northern Hemisphere ice volume. The northward westerly, in turn, encourages the EASM rain belt to move northward (He et al., 2021) and results in increases in the MMV of EASM rainfall (especially northern China). In addition, CO_2 acts as an internal feedback agent to AMOC changes (Barker et al., 2016). Under intermediate glacial condition, when the AMOC reaches a regime of bi-stability, rising CO_2 during Heinrich Stadial cold events can trigger abrupt transitions to warm conditions. Decreasing CO_2 during warm events leads to abrupt cooling transitions (Zhang et al., 2017). Therefore, CO_2 generally provides a negative feedback on MMV of EASM rainfall. During interglacial times decreasing ice volume, accompanied by reduced sea ice and more frequent freshwater perturbation, is correlated with lower frequency and smaller amplitude variability in abrupt climate events. The co-evolving GHG concentrations would further alter the sea surface temperature by greenhouse forcing, subsequently modulating the MMV.

Within the 100,000-year cycle, precession-band variability (4-5 cycles), characterized by increased insolation and atmospheric GHG, further heightens the positive response, leading to larger MMV of subtropical rainfall. Recent transient sensitivity experiments suggests that millennial-scale rainfall variability is driven primarily by meltwater and secondarily by insolation (He et al., 2021). During interglacial times under the combined influence of insolation and CO_2, model simulation shows that when insolation reaches the lower “threshold” value (between 358.2 and 352.1 W. m^{-2}), it triggers a strong abrupt weakening of the AMOC and results in abrupt cooling transitions over last 800 ka (Yin et al., 2021). Increased insolation could warm sea surface temperature and accelerate freshwater input from high latitude ice sheet as well as altering GHG concentration in the atmosphere (Lewkowicz and Way, 2019), which could, in turn, modulate MMV changes in the low latitude monsoon regions.

If both millennial-scale Ca/Ti and δ^{18}Osp represent subtropical rainfall amount, the modulation factors should be consistent. However, eccentricity, obliquity and precession bands MMV modulators differ for loess Ca/Ti and δ^{18}Osp, indicating they monitor different aspects of millennial-scale monsoon circulations. Modern observations and Lagrangian trajectories of air parcels in China during the summer monsoon indicate that moisture-induced precipitation doesn't derive from the strongest water vapor pathways (Sun et al., 2011; Jiang et al., 2017); local water vapor recycling contributes significantly to regional precipitation in East China (over 30%) and North China (exceeding 55%) (Shi et al., 2020). Hence, we speculate that δ^{18}Osp MMV monitors changes in the isotopic composition of rainfall, varying with changes in westerly transport paths associated with North Atlantic cooling events, consistent with the MMV of δ^{18}Osp being closely linked to winter insolation at 100- and 41- kyr periods and the absence of MMV modulation at precession band. We further hypothesize that Ca/Ti mainly represents the MMV in local rainfall amount, consistent with the MMV of tropical rainfall being more dynamically related to GHG and summer insolation at precession band.

In recent decades atmospheric GHG concentration is accelerating due to anthropogenic contribution of fossil fuels, suggesting that EASM (extreme) precipitation will increase as well. This inference is consistent with model simulations indicating that the number of extreme daily precipitation events and mean precipitation overall will increase significantly in response to higher GHG concentration (Dairaku and Emori, 2006). The anthropogenic GHG-evoked warming is projected to increase the lower-tropospheric water vapor content and enhance the thermal contrast between land and ocean (Kitoh et al., 1997). This will give rise to a northward shift of lower tropospheric monsoon circulation and an increase rainfall during the East Asian summer monsoon (Vecchi and Soden, 2007). Our results indicate that factors modulating EASM precipitation MMV in the past are consistent with those predicted to influence future changes in monsoonal precipitation, lending further confidence in those projections.

5. Conclusions

Our high-resolution loess Ca/Ti record displays millennial monsoon oscillations that persist over the last 650 ka. Wavelet results highlight remarkable GHG modulation at both 100 kyr and precession band as well as ice volume at 100 kyr period and local insolation forcing at precession band. The MMV of loess Ca/Ti and speleothem $\delta^{18}O$ are modulated by different orbital factors, implying that these two proxies document different climatic response of millennial-scale monsoon circulation. The inferred mechanism of how these internal and external factors modulate the MMV calls on dynamic linkages to variability in AMOC at both eccentricity and precession bands. In recent decades, atmospheric GHG concentration is dramatically increasing due to anthropogenic contribution of fossil fuels (Bousquet et al., 2006; Davis et al., 2010), resulting in accelerated melting of ice-sheets in bi-polar regions (Swingedouw et al., 2008; Golledge et al., 2019). Their combined effects lead to more frequent occurrences of extreme rainfall (Dairaku and Emori, 2006; IPCC, 2018). Our results indicate that the MMV EASM rainfall is modulated by ice volume, GHG, and insolation factors, consistent with those predicted to influence future changes in monsoonal precipitation.

CRediT authorship contribution statement

Fei Guo mainly contributes to the experiments, data analysis, idea and draft paper. Prof. Steven Clemens and Youbin Sun help to design the program and revise the draft. Huimin Fan assists to perform the experiments and data processing. Ting Wang, Yuming Liu and Xingxing Liu make contributions to the fieldwork and paper discussion.

Acknowledgments

We thank Xiaojing Du for offering idea on potential model test for this paper. This work was supported by grants from the Strategic Leading Research Program of Chinese Academy of Science (XDB40000000) and National Natural Science Foundation of China (41525008 and 41977173).

Declaration of Competing Interest

The authors declare that they have no known competing financial interests or personal relationships that could have appeared to influence the work reported in this paper.

References

Alvarez-Solas, J., Charbit, S., Ramstein, G., Paillard, D., Dumas, C., Ritz, C., and Roche, D. M.: Millennial-scale oscillations in the Southern Ocean in response to atmospheric CO_2 increase, Global Planet. Change, 76, 128-136, https://doi.org/10.1016/j.gloplacha.2010.12.004, 2011.

An, Z., Clemens, S. C., Shen, J., Qiang, X., Jin, Z., Sun, Y., Prell, W. L., Luo, J., Wang, S., Xu, H., Cai, Y., Zhou, W., Liu, X., Liu, W., Shi, Z., Yan, L., Xiao, X., Chang, H., Wu, F., Ai., L., and Lu, F.: Glacial-interglacial Indian summer monsoon dynamics, Science, 333, 719-723, https://doi.org/10.1126/science.1203752, 2011.

An, Z., Wu, G., Li, L., Li, J., Sun, Y., Liu, Y., Zhou, W., Cai, Y., Duan, A., Li, L., Mao, J., Cheng, H., Shi, Z., Tan, L., Yan, H., Ao, H., Chang, H., and Feng, J.: Global monsoon dynamics and climate change, Annu. Rev. Earth Planet., 43, 29-77, https://doi.org/10.1146/annurev-earth-060313-054623, 2015.

Bailey, I., Bolton, C. T., DeConto, R. M., Pollard, D., Schiebel, R., and Wilson, P. A.: A low threshold for North Atlantic ice rafting from "low-slung slippery" late Pliocene ice sheets, Paleoceanography, 25, PA1212, https://doi.org/10.1029/2009PA001736, 2010.

Barker, S., and Knorr, G.: A paleo-perspective on the AMOC as a tipping element, PAGES News, 24, 14-15, http://orca.cardiff.ac.uk/id/eprint/95186, 2016.

Beck, J. W., Zhou, W., Li, C., Wu, Z., White, L., Xian, F., Kong, X., and An, Z. A 550,000-year record of East Asian monsoon rainfall from ^{10}Be in loess. Science, 360, 877-881, https://www.science.org/doi/abs/10.1126/science.aam5825, 2018.

Bousquet, P., Ciais, P., Miller, J. B., Dlugokencky, E. J., Hauglustaine, D. A., Prigent, C., and White, J.: Contribution of anthropogenic and natural sources to atmospheric methane variability, Nature, 443, 439-443, https://doi.org/10.1038/nature05132, 2006.

Broecker, W. S.: Massive iceberg discharges as triggers for global climate change, Nature, 372 421-424, https://doi.org/10.1038/372421a0, 1994.

Cheng, H., Edwards, L., Sinha, A., Spötl, C., Yi, L., Chen, S., Kelly, M., Kathayat, G., Wang, X. F., Li, X. L., Kong, X. G., Wang, Y. J., Ning, Y.F., and Zhang, H. W.: The Asian monsoon over the past 640,000 years and ice age terminations, Nature, 534, 640-646, https://doi.org/10.1038/nature18591, 2016.

Clark, P. U., Marshall, S. J., Clarke, G. K., Hostetler, S. W., Licciardi, J. M., and Teller, J. T.: Freshwater forcing of abrupt climate change during the last glaciation, Science, 293, 283-287, https://doi.org/10.1126/science.1062517, 2001.

Clemens, S. C., Holbourn, A., Kubota, Y., Lee, K. E., Liu, Z., Chen, G., Nelson, A., and Fox-Kemper, B.: Precession-band variance missing from East Asian monsoon runoff, Nat. Commun., 9, 1-12, https://doi.org/10.1038/s41467-018-05814-0, 2018.

Cook, E. R., Anchukaitis, K. J., Buckley, B. M., D'Arrigo, R. D., Jacoby, G. C., and Wright, W. E.: Asian monsoon failure and megadrought during the last millennium, Science, 328, 486-489, https://doi.org/10.1126/science.1185188, 2010.

Dansgaard, W., Clausen, H. B., Gundestrup, N., Hammer, C. U., Johnsen, S. F., Kristinsdottir, P. M., and Reeh, N.: A new Greenland deep ice core, Science, 218, 1273-1277, https://doi.org/10.1126/science.218.4579.1273, 1982.

Dairaku, K., and Emori, S.: Dynamic and thermodynamic influences on intensified daily rainfall during the Asian summer monsoon under doubled atmospheric CO_2 conditions, Geophys. Res. Lett., 33, L01704, https://doi.org/10.1029/2005GL024754, 2006.

Davis, S. J., Caldeira, K., and Matthews, H. D.: Future CO_2 emissions and climate change from existing energy infrastructure, Science, 329, 1330-1333, https://doi.org/10.1126/science.1188566, 2010.

Golledge, N. R., Keller, E. D., Gomez, N., Naughten, K. A., Bernales, J., Trusel, L. D., and Edwards, T. L.: Global environmental consequences of twenty-first-century ice-sheet melt, Nature, 566, 65-72, https://doi.org/10.1038/s41586-019-0889-9, 2019.

Grinsted, A., Moore, J. C., and Jevrejeva, S.: Application of the cross wavelet transform and wavelet coherence to geophysical time series, Nonlinear Proc. Geoph., 11, 561-566, https://doi.org/10.5194/npg-11-561-2004, 2004.

Guo, F., Clemens, S. C., Wang, T., Wang, Y., Liu, Y., Wu, F., Jin, Z., and Sun, Y.: Monsoon variations inferred from high-resolution geochemical records of the Linxia loess/paleosol sequence, western Chinese Loess Plateau, Catena, 198, 105019, https://doi.org/10.1016/j.catena.2020.105019, 2021.

Guo, Z., Liu, T., Guiot, J., Wu, N., Lü, H., Han, J., and Gu, Z.: High frequency pulses of East Asian monsoon climate in the last two glaciations: link with the North Atlantic. Clim. Dynam, 12, 701-709, https://doi.org/10.1007/s003820050137, 1996.

He, C., Liu, Z., Otto-Bliesner, B. L., Brady, E. C., Zhu, C., Tomas, R., Clark, P. U., Zhu, J., Jahn, A., Gu, S., and Zhang, J., Nusbaumer, J., Noone, D., Cheng, H., Wang, Y., Yan, M., and Bao, Y.: Hydroclimate footprint of pan-Asian monsoon water isotope during the last deglaciation, Sci. Adv., 7, eabe2611, https://doi.org/10.1126/sciadv.abe2611, 2021.

Heinrich, H.: Origin and consequences of cyclic ice rafting in the northeast Atlantic Ocean during the past 130,000 years, Quat. Res., 29, 142-152, https://doi.org/10.1016/0033-5894(88)90057-9, 1988.

Hemming, S. R.: Heinrich events: Massive late Pleistocene detritus layers of the North Atlantic and their global climate imprint, Rev. Geophys., 42, RG1005, https://doi.org/10.1029/2003RG000128, 2004.

Hoegh-Guldberg, O., Jacob, D., and Bindi, M., et al.: Impacts of 1.5 C global warming on natural and human systems. Global warming of 1.5 C, An IPCC Special Report. IPCC Secretariat, 175-311, http://hdl.handle.net/10138/311749, 2018.

Huang, R., Chen, J., and Huang, G.: Characteristics and variations of the East Asian monsoon system and its impacts on climate disasters in China, Adv. Atmos. Sci., 24, 993-1023, https://doi.org/10.1007/s00376-007-0993-x, 2007.

Jiang, Z., Jiang, S., Shi, Y., Liu, Z., Li, W., and Li, L.: Impact of moisture source variation on decadal-scale changes of precipitation in North China from 1951 to 2010, Geophys. Res. Atmos., 122, 600-613, https://doi.org/10.1002/2016JD025795, 2017.

Kitoh, A., Yukimoto, S., Noda, A., and Motoi, T.: Simulated changes in the Asian summer monsoon at times of increased atmospheric CO_2, J.Meteorol. Soc. JPN. Ser. II, 75, 1019-1031, https://doi.org/10.2151/jmsj1965.75.6_1019, 1997.

Lai, Z. P., and Wintle, A. G.: Locating the boundary between the Pleistocene and the Holocene in Chinese loess using luminescence, Holocene 16, 893-899, https://doi.org/10.1191/0959683606hol980rr, 2006.

Lewkowicz, A. G., and Way, R. G.: Extremes of summer climate trigger thousands of thermokarst landslides in a High Arctic environment, Nat. Commun., 10, 1-11, https://doi.org/10.1038/s41467-019-09314-7, 2019.

Lisiecki, L. E., and Raymo, M. E.: A Pliocene-Pleistocene stack of 57 globally distributed benthic $\delta^{18}O$ records, Paleoceanography, 20, PA1003, https://doi.org/10.1029/2004PA001071, 2005.

Liu, J., Wang, B., Cane, M. A., Yim, S. Y., and Lee, J. Y.: Divergent global precipitation changes induced by natural versus anthropogenic forcing, Nature, 493, 656-659, https://doi.org/10.1038/nature11784, 2013.

Lo, L., Chang, S. P., Wei, K. Y., Lee, S. Y., Ou, T. H., and Chen, Y. C., et al.: Nonlinear climatic sensitivity to greenhouse gases over past 4 glacial/interglacial cycles, Sci. Rep., 7, 1-7, https://doi.org/10.1038/s41598-017-04031-x, 2017.

McManus, J. F., Oppo, D. W., and Cullen, J. L.: A 0.5-million-year record of millennial-scale climate variability in the North Atlantic, Science, 283, 971-975, https://doi.org/10.1126/science.283.5404.971, 1999.

Naafs, B. D. A., Hefter, J., and Stein, R.: Millennial-scale ice rafting events and Hudson Strait Heinrich (-like) Events during the late Pliocene and Pleistocene: a review, Quat. Sci. Rev., 80, 1-28, https://doi.org/10.1016/j.quascirev.2013.08.014, 2013.

Porter, S. C., and An Z. S.: Correlation between climate events in the North Atlantic and China during the last glaciation, Nature, 375, 305-308, https://doi.org/10.1038/375305a0, 1995.

Ramaswamy, V. et al.: Radiative forcing of climate change in Climate Change 2001: The Scientific Basis, Cambridge University Press, 349-416, https://csl.noaa.gov/assessments/ozone/1991/chapters/chapter7.pdf, 2001.

Shi, Y., Jiang, Z., Liu, Z., and Li, L.: A Lagrangian analysis of water vapor sources and pathways for precipitation in East China in different stages of the East Asian summer monsoon, J. Clim., 33, 977-992, https://doi.org/10.1175/JCLI-D-19-0089.1, 2020.

Sun, B., Zhu, Y., and Wang, H.: The recent interdecadal and interannual variation of water vapor transport over eastern China, Adv. Atmos. Sci., 28, 1039-1048, https://doi.org/10.1007/s00376-010-0093-1, 2011.

Sun, Y., Clemens, S. C., An, Z., and Yu, Z.: Astronomical timescale and palaeoclimatic implication of stacked 3.6-Myr monsoon records from the Chinese Loess Plateau, Quat. Sci. Rev., 25, 33-48. https://doi.org/10.1016/j.quascirev.2005.07.005, 2006.

Sun, Y., Clemens, S., Guo, F., Liu, X., Wang, Y., Yan, Y., and Liang, L.: High-sedimentation-rate loess records: A new window into understanding orbital-and millennial-scale monsoon variability, Earth-Sci. Rev., 103731, https://doi.org/10.1016/j.earscirev.2021.103731, 2021a.

Sun, Y., Clemens, S. C., Morrill, C., Lin, X., Wang, X., and An, Z.: Influence of Atlantic meridional overturning circulation on the East Asian winter monsoon, Nat. Geosci., 5, 46-49, https://doi.org/10.1038/ngeo1326, 2012.

Sun, Y., McManus, J. F., Clemens, S. C., Zhang, X., Vogel, H., Hodell, D. A., Guo, F., Wang, T., Liu, X., and An, Z.: Persistent orbital influence on millennial climate variability through the Pleistocene, Nat. Geosci., 14, 812-818, https://doi.org/10.1038/s41561-021-00794-1, 2021b.

Swingedouw, D., Fichefet, T., Huybrechts, P., Goosse, H., Driesschaert, E., and Loutre, M. F.: Antarctic ice-sheet melting provides negative feedbacks on future climate warming, Geophys. Res. Lett., 35, https://doi.org/10.1029/2008GL034410, 2008.

Thirumalai, K., Clemens, S. C., and Partin, J. W.: Methane, Monsoons, and Modulation of Millennial-Scale Climate, Geophys. Res. Lett., 47, e2020GL087613, https://doi.org/10.1029/2020GL087613, 2020.

Vecchi, G. A., and Soden, B. J.: Global warming and the weakening of the tropical circulation, J.

Clim., 20, 4316-4340, https://doi.org/10.1175/JCLI4258.1, 2007.

VanderPlas, J. T.: Understanding the lomb-scargle periodogram, The Astrophysical Journal Supplement Series, 236, 16, https://doi.org/10.3847/1538-4365/aab766, 2018.

Wang, Y., Cheng, H., Edwards, R. L., Kong, X., Shao, X., Chen, S., and An, Z. Millennial-and orbital-scale changes in the East Asian monsoon over the past 224,000 years, Nature, 451, 1090-1093, https://doi.org/10.1038/nature06692, 2008.

Yin, Q. Z., Wu, Z. P., Berger, A., Goosse, H., Hodell, D.: Insolation triggered abrupt weakening of Atlantic circulation at the end of interglacials, Science, 373, 1035-1040, https://doi.org/10.1126/science.abg1737, 2021.

Zhang, H., Griffiths, M. L., Chiang, J.C.H., Kong, W., Wu, S., Atwood, A., Huang, J., Cheng, H., Ning, Y., and Xie, S.: East Asian hydroclimate modulated by the position of the westerlies during Termination I, Science, 362, 580-583, https://doi.org/10.1126/science.aat9393, 2018.

Zhang, X., Knorr, G., Lohmann, G., and Barker, S.: Abrupt North Atlantic circulation changes in response to gradual CO_2 forcing in a glacial climate state, Nat. Geosci., 10, 518-523, https://doi.org/10.1038/ngeo2974, 2017.

Zhang, X., Lohmann, G., Knorr, G., and Purcell, C.: Abrupt glacial climate shifts controlled by ice sheet changes, Nature, 512, 290-294, https://doi.org/10.1038/nature13592, 2014.

Zhang, Z., Li, G., Cai, Y., Cheng, X., Sun, Y., Zhao, J., Shu, P., Ma, L., and An, Z. Millennial‐Scale Monsoon Variability Modulated by Low‐Latitude Insolation During the Last Glaciation. Geophys. Res. Lett., 49, e2021GL096773, https://doi.org/10.1029/2021GL096773, 2022.

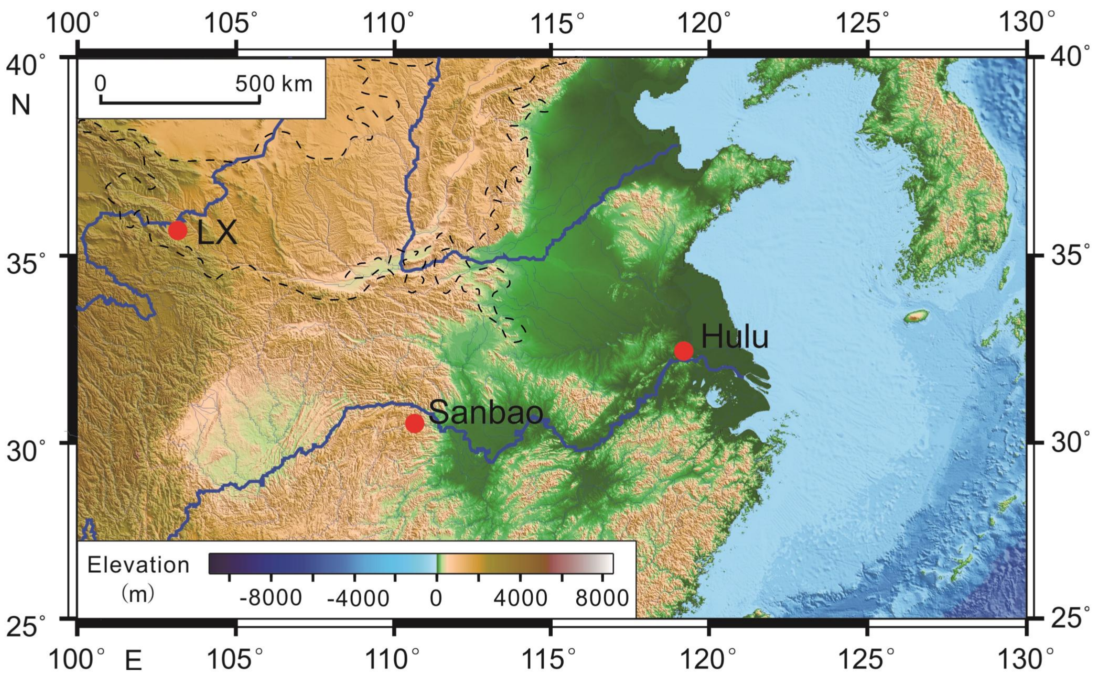

Figure. 1 The location of the Linxia (LX) loess profile and Hulu-Sanbao cave records. The Linxia profile, located on the edge of convergence zone for of alpine Qinghai-Tibet Plateau, northwest arid and the southeast monsoon area, is very sensitive to the migration of desert regions and monsoonal rainfall. Sanbao-Hulu cave is located in monsoon-influenced Yangtze River Valley, sensitive to the monsoon-induced precipitation changes. Black dash line represents the scope of Chinese Loess Plateau. The base map is drawn using GMT software, and the elevation data is from http://www.ngdc.noaa.gov/mgg/global/global.html.

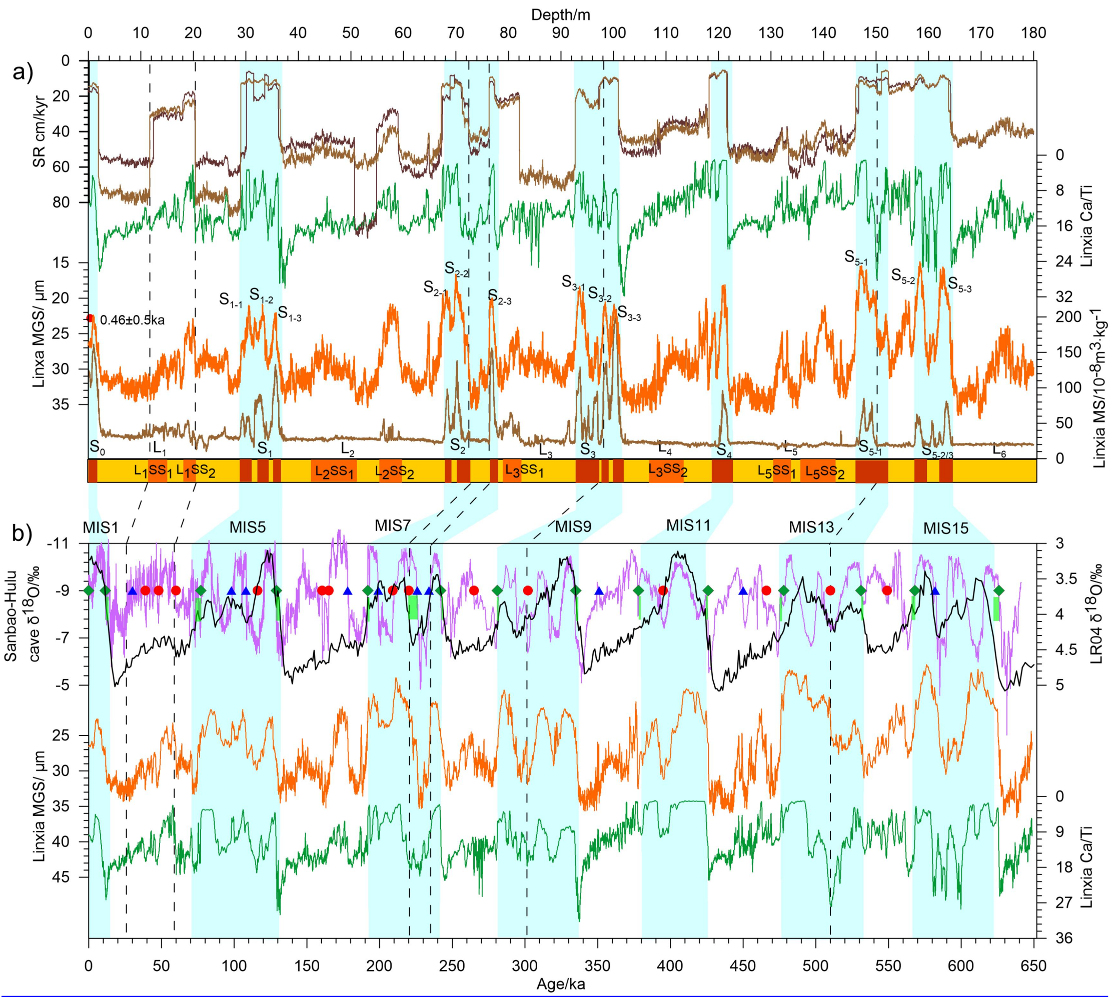

Figure 2 a) Strata and down-core variations of mean grain size (MGS), magnetic susceptibility (MS), Ca/Ti and sedimentation rate against depth (brown in benthic $\delta^{18}O$ age model and dark brown in speleothem $\delta^{18}O$ age model). Brown red, orange and yellow rectangles represent palaeosol layers, weakly pedogenic palaeosol in loess layers and loess layers, respectively. The timing of dash lines and glacial-interglacial transition are control points of benthic $\delta^{18}O$ chronology; b) Variations of MGS, Ca/Ti over last 650 ka and age model of Linxia loess section. Comparison of MGS and Ca/Ti in Linxia section with Sanbao-Hulu (Cheng et al., 2009, 2016) and benthic $\delta^{18}O$ stack (Lisiecki and Raymo, 2005). The dark brown squares, blue triangles and red dots represent the first (glacial-interglacial transition), second (precession cycles) and third (millennial-scale events) class age control points at the corresponding position of cave record, respectively (Sun et al., 2021a). Light blue bands donate the interglacial times. The short green rectangles represent the age differences between the two age models.

删除[SClemens]: tuning

删除[SClemens]: synchronized

删除[SClemens]: tuning

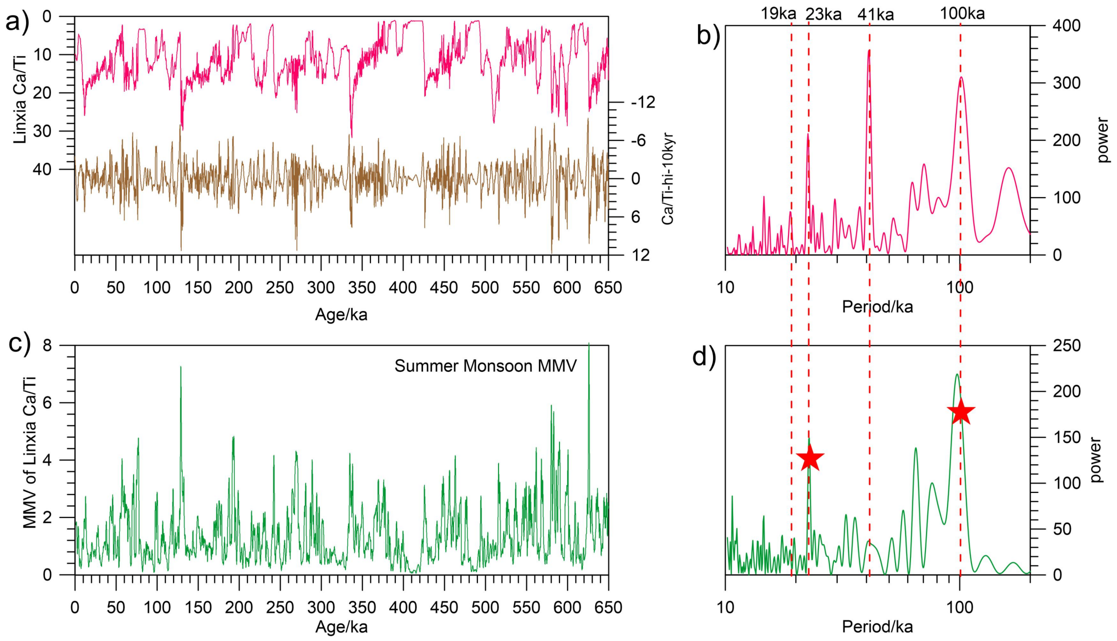

Figure. 3 Raw datasets, millennial-scale components (10 kyr high pass filtering signals) and MMV of the Linxia loess Ca/Ti record over the past 650 ka with their corresponding spectra. The orbital bands are marked with red dashed lines (eccentricity-100 kyr, obliquity-41 kyr ,precession-23 kyr and 19 kyr). Clearly variable eccentricity, obliquity and precession variances as well as persistent millennial-scale components are observed for loess Ca/Ti and MMV.

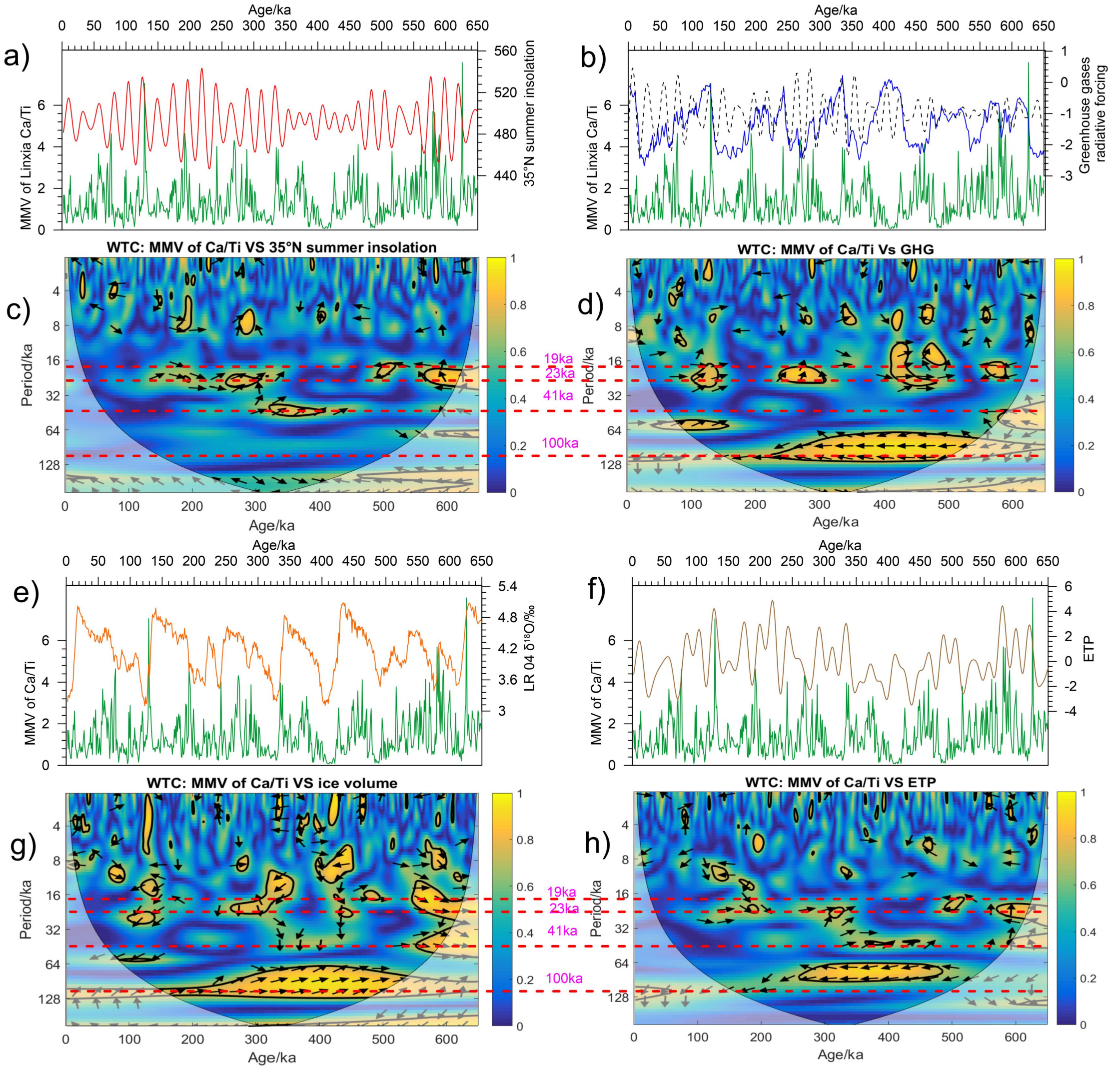

Figure. 4 Comparison of a) 35°N summer insolation forcing, b) GHG radiative forcing (black dish line donates the precession band-pass filtering results of ΔRF_{GHG}) and e) ice volume and f) ETP for MMV of Linxia loess Ca/Ti; Wavelet coherence between c) 35°N summer insolation, d) GHG radiative forcing, g) ice volume, h) ETP and MMV of loess Ca/Ti over the past 650 ka. The orbital bands are marked with red dashed lines (eccentricity-100 kyr, obliquity-41 kyr , precession-23 kyr and 19 kyr). The orange color indicates strong correlation for the two time series. The black lines plot coefficients of determination is more than 0.76. The black arrows represent the phrase relationship with rightward, upward and downward arrows indicating in-phrase, leading and lagging phrase, respectively. Strong eccentricity, weak obliquity and precession bands ice volume modulation are observed for MMV of loess Ca/Ti. Strong eccentricity and precession bands GHG modulation as well as weak summer insolation forcing are detected for MMV of loess Ca/Ti.